Pavement testing by integrated geophysical methods: Feasibility, resolution and diagnostic potential

CrossMark

Luciana Orlando, Ettore Cardarelli, Michele Cercato, Giorgio De Donno *, Luca Di Giambattista

"Sapienza" University of Rome – DICEA, Via Eudossiana 18, 00184 Rome, Italy

ABSTRACT

This work is focused on the assessment of the diagnostic potential of several geophysical methods when applied to the investigation of a rigid airport pavement. The potential and limit of each technique are evaluated as well as the added value deriving from their integration. Firstly, we reconstruct a high-resolution image of the pavement by a large electromagnetic and georadar screening. An advanced processing of georadar data, implemented through the picking of the arrival times of reflections for each profile, provides a quantitative estimation of the deviation between the design and the as-built thickness of layers. Additionally, electrical tomography has been applied to unequivocally identify the anomalous zones, where higher values of resistivity would be associated to porous zones that are prone to degradation and failure. The seismic tomographic survey had the additional purpose to recover the mechanical properties of the pavement in terms of both P- and S-waves and consequently of elastic constants (Poisson's ratio), whose values were consistent with those recovered in literature. The anomalies detected by each technique are consistent in their indications and they can be correlated to failure phenomena occurring at layer interfaces within the pavement structure or to unexpected variations of the layer thicknesses. The cost-effective geophysical campaign has validated the four-layered system deduced from the original design and has been used to reconstruct a high-resolution map of the pavement in order to discriminate fractures, crack-prone areas or areas where the as-built differs from the original design.

© 2016 Elsevier B.V. All rights reserved.

1. Introduction

During their life cycle, airfields and aircraft runways must preserve the structural integrity for obvious safety and economic reasons. An effective maintenance program should avoid cracking and failures and minimize time and costs for ordinary servicing operations. In light of this, all reliable information for monitoring the conservation status of the pavements are relevant to identify any failure-prone areas.

Over the last decades, geophysical methods have been affirmed as one of the most used non-destructive methods, with the primary aim to assess the thickness of the pavement layers and to give an estimation of physical and mechanical parameters of the pavement, even though mainly involving only the application of Ground Penetrating Radar (GPR) and Falling Weight Deflectometer (FWD).

GPR has been extensively used for over twenty years now to assess the conservation status of road pavements (e.g Saarenketo, 1997), to evaluate the effective thickness of different layers (e.g Saarenketo and Scullion, 2000; Al-Qadi and Lahouar, 2005; Loizos and Plati, 2007; Liu and Sato, 2014), to investigate the *as-built* conditions (e.g Maser et al., 2006), to assess the amount of water and clay in the subsoil (e.g Benedetto and

Benedetto, 2011; Benedetto and Tosti, 2013; Benedetto et al., 2012) and to monitor cultural heritage (e.g Vaughan, 1986; Malagodi et al., 1996; Neubauer et al., 2002; Orlando and Slob, 2009). When compliant to existing standards for testing concrete or asphalt surfaces (American Society of Testing Materials, 2008), GPR measurements can be executed without disturbing the operability of roads. Maser et al. (2006) have demonstrated that the ground-coupled GPR system has difficulty resolving thin uppermost layers (<100 mm), whereas air coupled antennas achieved an increased resolution and can differentiate thinner layers (about 50 mm for asphalt pavements). When compared with air-launched systems, the ground-coupled system has the distinctive advantage of a significant increase in depth of investigation, though ground-coupling limits the speed of vehicles and productivity (Al-Qadi and Lahouar, 2005; Maser et al., 2006). GPR measurements may be affected by other limitations: there is an intrinsic inability to clearly differentiate between layers of similar materials due to the low contrast in their dielectric properties (Al-Qadi et al., 2001) and additionally the presence of salt, water or high iron content in slag aggregates may be responsible for high attenuation of the electromagnetic signal in some pavement layers. As such, the analysis results may be misleading sometimes, especially for concrete pavements (Maser et al., 2006; Al-Qadi et al., 2001; Mesher et al., 1995; Gordon et al., 1998). Resolution of recorded data is enhanced by using high frequency antennas, but at the expense of the penetration

* Corresponding author.
  E-mail address: giorgio.dedonno@uniroma1.it (G. De Donno).

depth, which is reduced when the frequency increases (Al-Qadi and Lahouar, 2005; Loizos and Plati, 2007; Gordon et al., 1998).

Beside the GPR method, there are other non-destructive methods widely used during the last decades, to evaluate the stiffness and the structural capacity of pavement sand soil foundations. One of the most used for rigid pavements is the FWD, which is an apparatus designed to impart a load pulse to the pavement surface by dropping a standard weight from a constant height on a circular load plate firmly placed on the pavement. The deflection induced by the impact is measured at several distances and used to calculate stiffness-related parameters of the pavement structure through various back-calculation processes (e.g Seo et al., 2009; Tholen et al., 1985). In spite of being a relatively rapid method, the FWD is very heavy and expensive and its use is limited to few companies. In light of this, a German roadway organization has developed a Portable Falling Weight Deflectometer (PFWD), a lightweight instrument, employing the same principles of FWD with correlations between dynamic deflection modulus and bearing capacity of layers made easy (e.g Kim et al., 2007).

For estimating the stiffness and structural bearing of road pavements, Dynamic Cone Penetrometer (e.g De Beer, 1990; Mohammadi et al., 2008) has also been employed, while Infrared Thermography (e.g Moropoulou et al., 2001; Clark et al., 2003) can help to detect delaminations or near surface defects.

Seismic methods have also been proved useful for field testing of pavements (e.g Nazarian et al., 1654), because the elastic modulus, the shear modulus and the Poisson's ratio can be calculated without any empirical correlation from the seismic velocities (P-wave and S-wave velocities). From this point of view, the pavement testing with surface waves (Ryden and Park, 2006) can provide reliable 1D models of seismic velocities up to significant depths, even though the resolution could be lower with respect to the refraction/reflection seismic methods. Many applications of this technique for pavements are reported in literature (e.g Ryden and Park, 2006; Ryden et al., 2004; Goel and Das, 2008), although it has been demonstrated that an effective characterization is achieved with datasets exhibiting a frequency of few tens of kHz, which is something not achieved by conventional geophysical instrumentation (with geophones up to 100 Hz).

Although Electrical Resistivity Tomography (ERT) is a well-known technique for archaeological prospection involving buried structures (e.g Cardarelli et al., 2008; Tsokas et al., 2008; Papadopoulos et al., 2010; Tsourlos and Tsokas, 2011), only a few references available in the scientific literature concern the application of DC electrical methods for the characterization of pavements (e.g Buettner et al., 1996). This technique has the considerable advantage of investigating a significant volume of subsoil (up to 0.25 times the maximum spread of the ERT array) with good resolution and reliability, even though the deployment of electrodes and the measurement time heavily affect productivity. ERT is diagnostic method to detect porous zones that are prone to degradation or failure anomalous zones, both characterized by an increasing resistivity comparing with the background medium.

It is well-know that multi-technique approaches integrating data from different methods may improve the reconstructed image of the pavement (e.g Piro et al., 2003; Orlando, 2005; Drahor, 2006; Cardarelli et al., 2014) although the accuracy, reliability, cost-effectiveness and rapidity are key issues to fully exploit the diagnostic potential of non-destructive testing methods.

The evaluation of the structural integrity of pavements calls for high-resolution investigation of the pavement layers and adequate depth of penetration to properly characterize the infrastructure and underlying soil. Our approach is based on a preliminary extensive screening performed by low frequency electromagnetic (EM) and GPR followed by a more focused survey encompassing ERT and seismic refraction tomography (SRT).

The idea is to point out possible defects and anomalous zones by a first screening consisting of measures which are low-cost, rapid to execute and fast to interpret.

This procedure has been tested on an airfield apron located in central Italy, whose current conditions must be assessed to define the planned and condition based maintenance and repair.

On these basis, the main goals of the integrated geophysical investigations at this site are:

- to individuate the differences (if any) between the original and the as-built design;
- to detect and to characterize anomalous and weakness zones within the different layers of the pavement;
- to give an estimation of the physical and mechanical parameters of the different layers;
- to assess the diagnostic potential and the main limits of each single geophysical techniques and the added value of the proposed integrated procedure.

In the following four sections we will firstly describe the investigated site (section no. 2), providing then technical information about the geophysical methods employed (section no. 3), presenting the results of the single technique and the added value of the integrated approach (section no. 4) with a final discussion (section no. 5).

2. Site description

The study area is a 18 m wide and 50 m large apron, located within an airport in central Italy (Fig. 1). According to its original design, the apron consists of four layers (Fig. 2a): Portland Cement Concrete (PCC) slabs up to 30 cm of depth (maybe fiber reinforced), a base layer of 20 cm (probably stabilized aggregate), a 40 cm thick subbase layer (often made of lower quality materials than the base course) and a 60 cm thick subgrade (in situ compacted soil). A picture of the under construction apron is given in Fig. 2b (left). The shallower in-situ deposits consists of Pleistocene silty sand overlying Pleistocene silty clay, with variable thickness, as confirmed by an exploratory borehole drilled close to the study area.

A couple of fractures resulting from longitudinal distress were observed by visual inspection on the apron surface, as reported in Fig. 2b (right). The cracks are directed along the y-direction, joining the opposite sides of a single slab. The longitudinal cracking is usually due to the combination of cycled loads as it can indicate structural failure due to subsidence or cracking phenomena occurring within or at the interface of the underlying layers. Therefore, the airport Authority needs to extensively
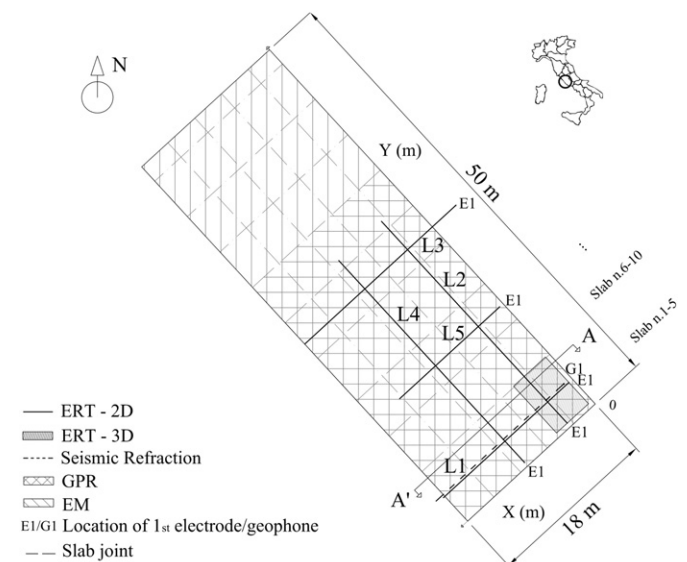

Fig. 1. (a) Aerial plan of the surveyed areas and location of the field investigations.
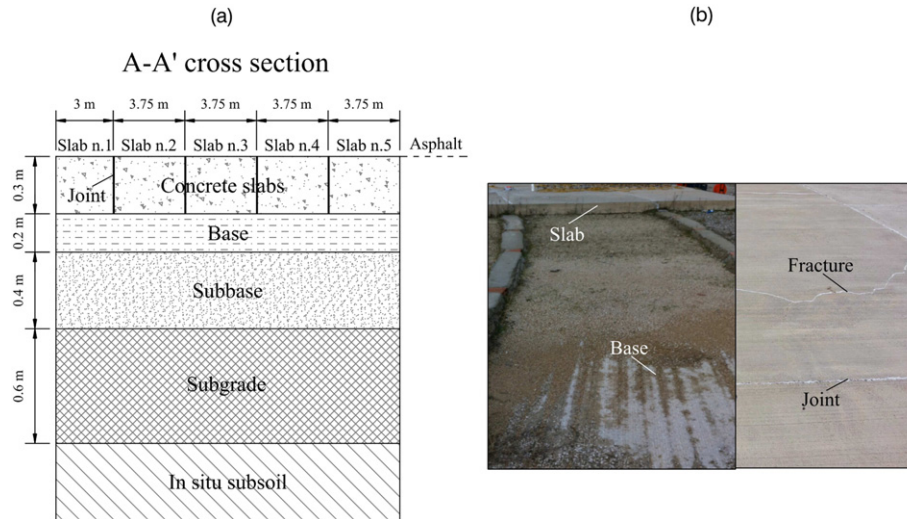
(b)

A-A' cross section

Fig. 2. (a) A-A' cross-section as indicated in Fig. 1. (b) Picture of the under-construction apron (left) with indication of joints and fractures (right).

map this area for planning the restoration activities and steering the repair works towards a partial or a full depth reconstruction.

3. Methods, data acquisition, processing and inversion

The proposed investigation procedure involves the sequential application of EM, GPR, ERT and SRT techniques. The main aspects of each technique is hereby detailed by paragraph. The parameters employed for field data acquisition are reported in Table 1.

3.1. Low-frequency electromagnetic (EM)

The low frequency electromagnetic campaign was performed within a 18×50 m rectangular grid, where 0.5 m spaced profiles were acquired along both the x- and y- direction (Fig. 1), using three different frequencies (2, 8 and 16 kHz). For each frequency, the recorded output consists in the complex mutual coupling ratio (Q^*) between the secondary and the primary magnetic fields, expressed in parts per million [ppm] for both the in-phase and quadrature components.

Table 1
Parameters for field data acquisition.

Technique	Acquisition details
Low-frequency electromagnetic (EM)	Device: Electro-magnetometer GSSI Profiler EMP 400 Frequencies: 2, 8 and 16 kHz Grid spacing: 0.5 m Investigated area: 18×50 m
Ground Penetrating Radar (GPR)	Device: IDS antennas Frequencies: 200, 600 and 900 MHz Grid spacing: 0.5 m Investigated area: 18×32 m
Electrical Resistivity Tomography (ERT)	Device: Iris Syscal Pro resistivimeter Array: Dipole-dipole roll-along (customized sequence) 2D lines, Dipole-dipole 16×3 snake array (3D grid) Electrodes: 48 copper plates (10×10 cm) Electrodes spacing: 0.3 m Investigated area: 4.5×6.6 m (3D) and five 2D lines (L1–L5)
P- and SH-wave Seismic Refraction Tomography (SRT)	Device: 2 seismographs Geode Geometrics Seismic source: 1 kg sledge-hammer and steel/wood-aluminum plates Geophones: 36 geophones at 8 Hz (P-wave) and 48 geophones at 40 Hz (S-wave) Geophones spacing: 0.3 m Shots distance: 0.3 m Investigated area: L1 line

Under certain constrains, technically defined as "operation at low-values of induction number" the quadrature component is only a function of the inter-coil spacing s, the operating frequency f and the ground conductivity σ (McNeill, 1980). The induction number θ is defined as:

$$\theta = \sqrt{\frac{2\pi f \mu_0 \sigma s^2}{2}} \tag{1}$$

where μ_0 is the magnetic constant or permeability of free space.

The above hypothesis holds for $\theta \ll 1$. In this case θ ranges from 0.001 to 0.01, for the whole range of frequencies. Therefore the apparent conductivity σ_a is given by:

$$\sigma_a = \frac{4}{2\pi f \mu_0 s^2} Im(Q^*) \tag{2}$$

The in-phase component is generally very sensitive to the presence of metallic objects. When the complex ratio Q^* is mapped as a function of the induction number, a "resistive-limit zone" can be individuated as the area where the magnetization effect dominates the EM response. Within this zone (corresponding to low θ values) Q^* becomes real and its in-phase component depends directly to the half-space magnetic apparent susceptibility κ, as follows (Won and Huang, 2004):

$$Re(Q^*) = -\frac{\kappa}{2+\kappa} G \tag{3}$$

$$\kappa = -\frac{2Re(Q^*)}{[Re(Q^*) + G]} \tag{4}$$

where G is a variable that depends only on the coil configuration. In particular for bistatic horizontal coplanar coils, G can be expressed as:

$$G = -\frac{8\left(\frac{h}{s}\right)^2 - 1}{\left[4\left(\frac{h}{s}\right)^2 + 1\right]^{5/2}} \tag{5}$$

being h the height of the sensor.

Under the above assumptions, we provide maps of both the apparent electrical conductivity and the apparent magnetic susceptibility of the investigated underground, after despiking the raw data.

3.2. Ground Penetrating Radar (GPR)

Similarly to the EM investigation, the 0.5 m spaced GPR profiles were acquired within a 18 × 32 m rectangular grid (Fig. 1). Three different frequencies (200, 600 and 900 MHz) were employed to investigate with different resolution the pavement structure and foundation, which has a limited thickness and exhibits similar electromagnetic characteristics among the different layers. The 200 and 600 MHz shielded antennas were simultaneously acquired and data have been recorded on 3 channels (channels 1 and 2 where both antennas act as transmitter and receiver and channel 3 where the signal is transmitted by the 200 MHz antenna and received by the 600), while a single-channel acquisition was performed with the 900 MHz antenna.

The recorded signals were firstly processed by moving the start time and applying a band-pass filter, with lower and upper cut-off frequencies of 100–500, 100–1000 and 100–1900 MHz, for 200, 600 and 900 MHz antennas respectively. Further processing includes a linear gain for equalizing the signal amplitude and recovering the energy losses with depth and a background removal for suppressing coherent noise. The three-dimensional data cube built with the GPR profiles was used to extract time-slices (horizontal sections of the energy at different times) in order to map the subsurface targets. The time-slices are built summing the squared normalized absolute amplitude, proportional to the back-scattered (reflected and diffracted) energy (for the sake of simplicity we have marked it as reflected energy in the following sections), within a fixed time window. For the time-depth conversion, the EM wave velocity was determined by diffraction hyperbola fitting. This procedure has been applied at regular steps within the site - each 10 profiles (5 m) in both directions - and at depths ranging from 0.3 and 0.9 m. The resulting mean velocity is 10 cm/ns with a standard deviation of approximately 1 cm/ns.

The thickness of the pavement layers were derived from picking of the times of the main reflections for each profile direction (longitudinal and transversal) and for each antenna frequency, obtaining the values of x, z and t related to the trace position in the layer. Using a velocity of 10 ± 1 cm/ns we calculated and mapped the thickness of the first two layers and the depth of the subgrade-subsoil interface. The maps were obtained by overlapping the data of longitudinal and transversal profiles for each frequency.

3.3. Electrical Resistivity Tomography (ERT)

Five 2D ERT lines (L1–L5) were performed on the study area (Fig. 1) using 48 copper electrodes spaced 30 cm apart and a dipole-dipole array configuration taking advantage of the roll-along acquisition technique. Under the site conditions, the dipole-dipole array combines consistent signal strength with good resolution and depth of investigation. The chosen electrodes are completely non-invasive as we employed a 10 cm square copper plates (Fig. 3a). The L3 line is partially located outside the apron (Fig. 1).

2D ERT pseudosections are inverted using the VERDI algorithm (Cardarelli and Fischanger, 2006) which is based on the formalism of inequality constraints that allows easy introduction of a priori information into the inversion process. In this particular case, we made no preliminary assumption on the pavement layering. This code is now capable to perform robust inversion (Wolke and Schwetlick, 1988) in addition to the standard inversion procedure and to automatically select the optimum damping value minimizing the Absolute Error for each iteration (De Donno, 2013). The quality of the acquired dataset and of the inversion procedure is proven by the very low Absolute Errors (1.65% and 3.09%) of the final models described in Section 4.

A smaller area of the apron was investigated by using a 3D ERT configuration (Fig. 3b), where the 48 electrodes are arranged into a 16 × 3 snake acquisition scheme. Repeating 11 times this scheme leads to a global inspected zone of 4.5 × 6.6 m, with 0.3 m spaced electrodes. The overall dataset to be inverted consists of about 32,000 apparent resistivity data. The 3D ERT data was inverted using the ErtLab© commercial software by Multi-Phase Technologies, LLC and Geostudi Astier.

3.4. Seismic refraction tomography (SRT)

As described in Section 1, the seismic survey has the additional purpose to recover the mechanical properties of the pavement in terms of both P- and S- wave velocity and additional of relevant elastic constants (e.g. Young's modulus, Poisson's ratio, etc.).

Seismic data were recorded along the L1 line (Fig. 1), employing a 36 channel system of 40 Hz vertical geophones (see Table 1) for P-waves while a 48 channels system were used with 14 Hz horizontal geophones for SH-waves. Additional shots were fired within the array spread, if compared to standard refraction survey, to permit a high resolution (HR) tomographic reconstruction (Fig. 3c).

For SH-waves acquisition, we employed a lightweight wood/aluminum source that allows horizontal hammer impacts in opposite directions, to enhance the picking of the S-wave arrival by phase difference (Fig. 3d), while the P-wave was generated by a 1-kg hammer impact on a steel plate.

Both acquisitions have been performed with a geophone streamer, made up by abrasion-resistant steel tripod plates connected and towed by a high tensile-strength band.

Inversion of seismic tomography data was performed using the algorithm described in (Cardarelli and de Nardis, 2001), employing the linear travel time interpolation (LTI) method for ray-tracing (Asakawa and Kawanaka, 1993) and the iterative biconjugate gradient algorithm for traveltime inversion (Cardarelli and Cerreto, 2002).

4. Results

According to the theory, the lowest frequency (2 kHz) was used to map the apparent susceptibility, while the apparent conductivity map was derived from the 16 kHz dataset. The apparent conductivity (Fig. 4a) pointed out two main anomalous zones: a low conductive area located at y = 6–18 m and x = 10–28 m (marked as A) and a high conductive area extended along the x-direction at y = 0–3 m (marked as B). The anomaly marked as B was detected also in the apparent susceptibility map (Fig. 4b), approximately with the same geometrical characteristics, and due to the high conductivity and high-susceptibility displayed, it could be related e.g. to an increase of the water content or to a reinforced structure (road, concrete pavement, etc.). In this case we can confirm that this anomaly is due to a pre-existent pavement through the analysis of the original working plans. Although a good lateral resolution can be achieved through EM measurements, this method has the considerable disadvantage of a low vertical resolution as it provides only average apparent values of the whole investigated volume.

Using the GPR data, we made a step forward towards the increment of the vertical resolution. An example of a GPR profile acquired at y = 0.5 m, is reported in Fig. 5, for the 200 (Fig. 5a), 600 (Fig. 5b), 200–600 (Fig. 5c) and 900 (Fig. 5d) MHz antennas. The best resolution was achieved through the 900 MHz antenna (Fig. 5d) as long as it is focused only on the shallower part of the pavement (slab, base and subbase, marked in yellow, orange and green respectively in Fig. 5). The deeper part of the pavement system (interface between subgrade and subsoil, marked in purple in Fig. 5) can be characterized by the 200–600 MHz antennas. The 900 MHz GPR profiles related to the L1 and L3 alignments (Figs. 6a and 7a) confirm that the pavement is effectively formed by a four-layer system, where the slabs are always well detectable, with a thickness of about 30 cm. A higher signal attenuation, maybe due to an increase of conductivity, occasionally prevent the detection of the third layer. The high reflectivity displayed at x = 0–5 m is probably due to the presence of the preexisting structure located below the sub-base layer, previously identified by the EM method.
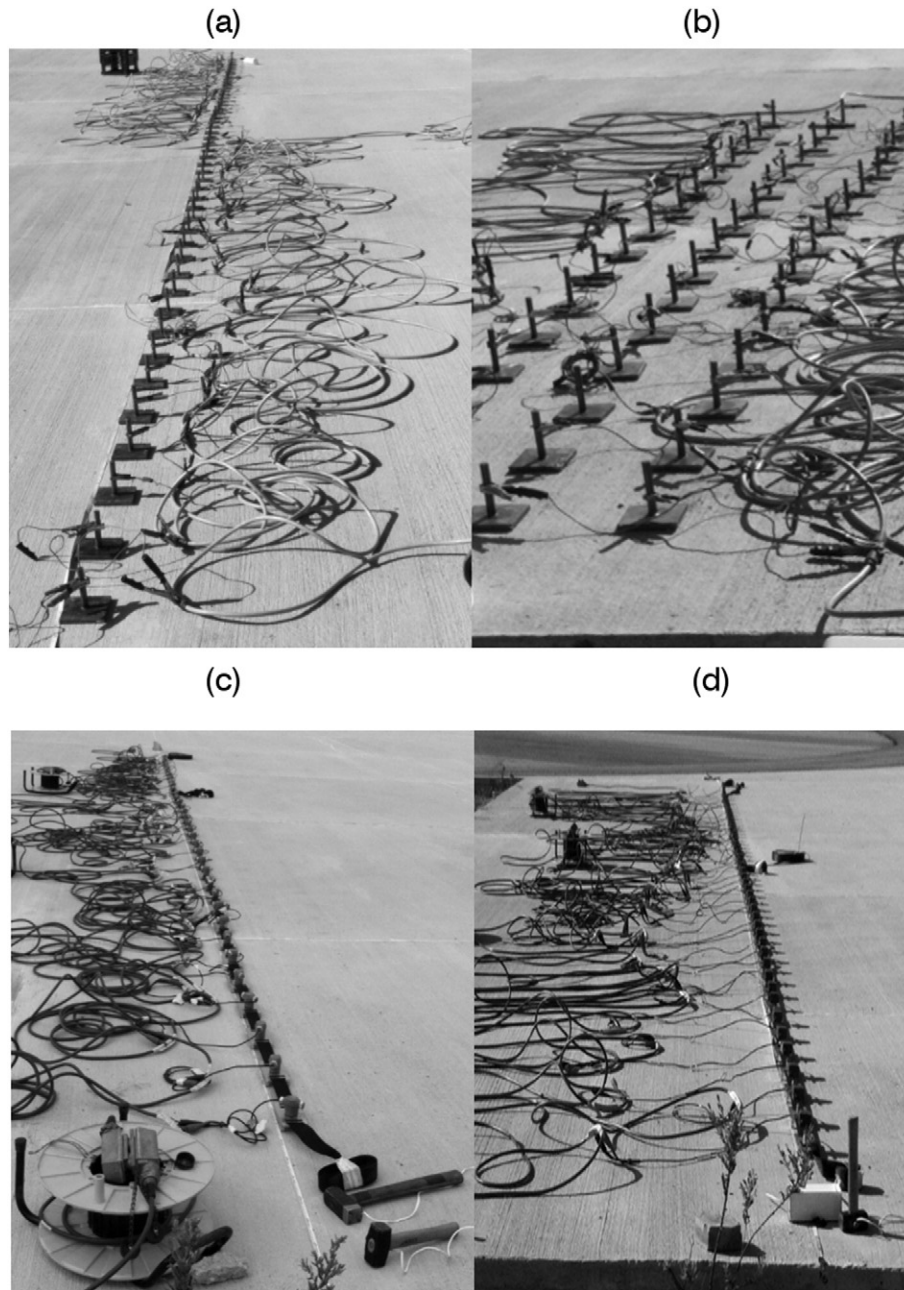
Fig. 3. (a) 2D ERT and (b) 3D ERT arrays, by using non-invasive 10 cm square copper plates. (c) P-Wave acquisition and (d) SH-Wave acquisition on line L1 in Fig.1a, by using a geophone streamer (three-legged steel plate) and lightweight sources.

Where GPR data are mapped as time-slice (Fig. 8), we can discriminate the different response among the various materials in terms of reflected energy. For the sake of completeness, we present in Fig. 8 four time-slices, related to increasing depths (0–30 cm; 30–60 cm; 60–90 cm; 90–120 cm) and different antenna frequencies: 900 MHz (Fig. 8a, b and c) and 200 (transmitting)-600 (receiving) MHz (Fig. 8d). In detail the time-slice in Fig. 8a is able to detect the slab joints (black arrows) and the variation of intensity of reflected energy among the different slabs. The anomalous high-reflected energy zone (A) in Fig. 8b and c, superimposed to the EM resistive anomaly (A in Fig. 4a), is probably related to a non-homogeneous composition of base or subbase layers. Furthermore we can argue that the base and subbase layers are built with resistive material having a grain dimension similar to the antenna wave length, causing diffraction phenomena seen as backscattering energy in Fig. 8b,c. When the deeper subgrade is analyzed (Fig. 8d), the main anomaly (B), probably due to a reinforced pre-

existent structure, is y-directed similarly to the EM evidences (Fig. 4). The GPR results are much more detailed with respect to EM both in terms of spatial and vertical resolution of the pavement layers, whereas the time needed for investigating the apron remains approximately the same for both methods. On the other hand EM allows to characterize the structure in terms of magnetic susceptibility of the material.

When the GPR dataset is used to map as a function of depth of the thickness and interfaces between layers (Fig. 9), through the advanced processing described in Section 3.2, we can have a quantitative estimation of the deviation between the as-built and the design thicknesses of the layers and to give a causal relationship for the detected anomalies. The thickness of the concrete slab is shown in Fig. 9a. The maximum interval, around the nominal thickness of 30 cm, is about 25–45 cm, with an absolute error, derived from the wave velocity estimation, around 3 cm. More specifically, the white line in Fig. 9a includes a large area (corresponding to the A-zone in Fig. 8b) where the slabs are slightly
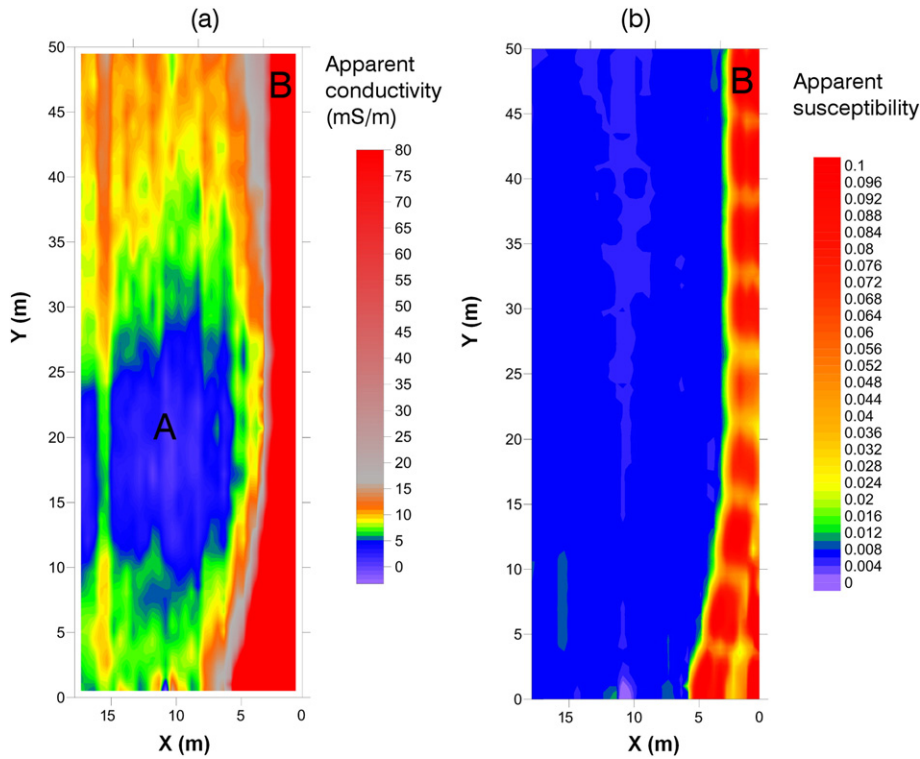
Fig. 4. Map of the EM results. (a) Conductivity map for the 16 kHz frequency with indications of resistive (A) and conductive (B) zones. (a) Magnetic susceptibility map for the 2 kHz frequency with indications of the anomalous zone (B).

thinner than the planned ones. However, we can also identify zones where the thickness of the slabs are larger than 40 cm, even if small-sized. The thickness of the base layer (Fig. 9b) is characterized by a
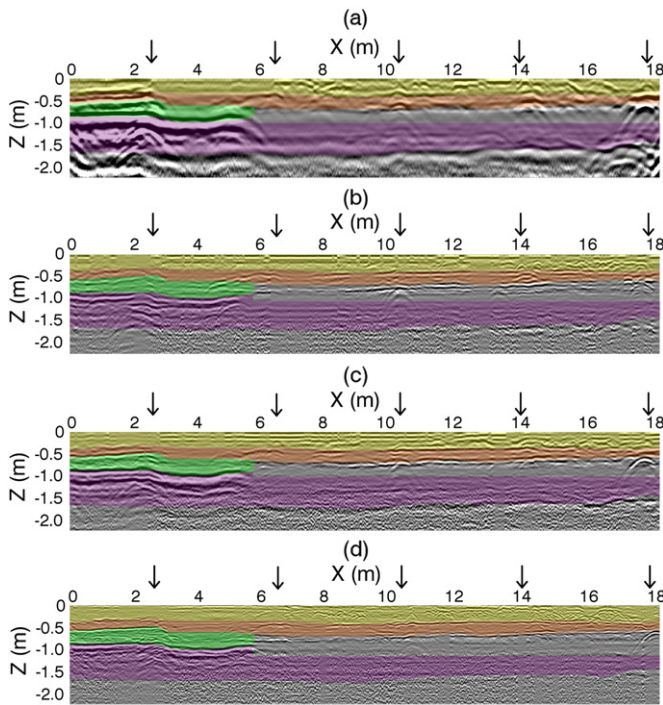

Fig. 5. Example of GPR profiles at y = 3.5 m (corresponding to the L1 line in Fig. 1a), for the 200 (a), 600 (b), 200–600 (c) and 900 (d) MHz antennas. The layers are marked in yellow (slabs), orange (base), green (subbase) and purple (subgrade).

wider variation (2–36 cm), even though the prevalent values are about the order of 16–20 cm, consistent with the original design. In this case the layer thickness is biased by about 5 cm. The thickness of the whole pavements system (Fig. 9c), corresponding to the depth of the subgrade-subsoil interface, ranges between 120 (corresponding to the B-zone) and 190 cm, with a maximum error in the thickness estimation of ±15 cm. This interface is not always visible in the study area.

Starting from these results, we calibrated the second part of the geophysical campaign, with the dual purpose to characterize with an ERT survey the deeper part of the pavement (including the foundation soil) and to give an estimation of the elastic parameters of the subsoil through high-resolution seismic tomography.

The inverted ERT model obtained for the L1 line (Fig. 6b) was able to reconstruct the four layers of the pavement structure: the PCC slabs have a conductive behavior (30–40 Ωm) since they are probably made of a Fiber Reinforced Concrete (concrete with discontinuous or uniformly dispersed fibers). In fact, the carbon or polypropylene fibers, often used for increasing the ductility of concrete elements and the resistance to impact load of apron pavements, exhibit a slightly conductive behavior (e.g. about 13 Ωm after Moskalyuk et al., 2012). The lack of the typical rebar reflections on the corresponding GPR profile (Fig. 6a) confirms the absence of a continuous steel reinforcing throughout the pavement. On the contrary, the base layer has a resistivity ranging from 200 to 600 Ωm, and the subbase is relatively conductive (60–80 Ωm). The subgrade is moderately resistive (>300 Ωm), while the underlying in-situ subsoil has a resistivity value of about 30–40 Ωm. In the first part of the line (x = 2–6 m, corresponding the slab. n.2) the effective layering is quite different with respect to the adjacent layers, due to the presence of the pre-existent structure.

The L3 ERT line (Fig. 7b) is partially located outside the apron; the inversion outcome for this line confirms the reliability of this technique to resolve the four-layered configuration of the pavement and to give information about the type of anomalies already individuated by GPR. The concrete slab situated at x = 7–10.75 m, seems to be thinner than the neighboring ones and consequently the presence of a high-energy
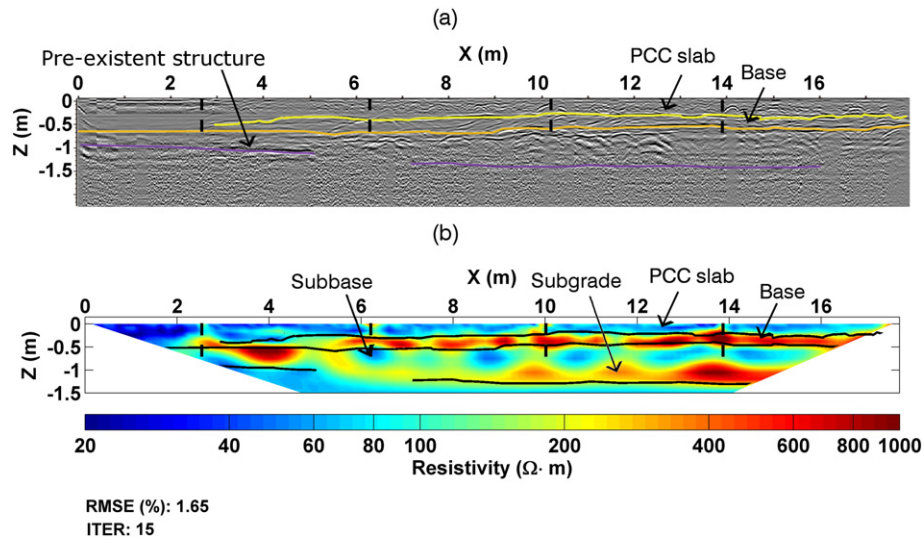
Fig. 6. (a) GPR vertical profile on L1 line for the 600 MHz antenna. The layers are marked in yellow (slabs), orange (base), green (subbase) and purple (subgrade). (b) Inverted model of ERT line L1. The direction of the line and the position of the first electrode is shown in Fig. 1. The layers are marked in black. Slab joints are indicated by dashed lines.

area in the respective GPR time-slices (Fig. 8a and b) could be clarified. The resistivity of the deeper layer, situated at a depth of 0.9–1.3 m, reaches values higher than 2000 Ωm at x = 0–3 m (area marked as B in Figs. 4 and 8d) and at x = 10–15 m. The latter anomaly has been not identified by the other techniques.

When compared to the GPR results, the ERT model is capable to explore up to 1.5 m of depth so that the deeper anomalies are better resolved. In addition to this, we can have additional information about the presence of fractures or cracking-prone zones, generally associated to higher resistivity values. Nevertheless GPR profiles and ERT lines describe a similar scenario both in terms of effective layering (thickness and depth) and for the detection of anomalies, where GPR holds a better resolution for the shallower anomalies and the ERT is able to investigate deeper targets.

From this point of view higher resolution can be given by the 3D ERT array (eleven array each formed by 16 × 3 electrodes spaced 30 cm apart), focused on the bottom-right part of the pavement in Fig. 1. The inverted model mapped as horizontal slices at 15 cm (Fig. 10a) and 40 cm (Fig. 10b), shows both the slab joints (Fig. 10a) and two deeper

anomalous resistive zones located at x = 0–2.5 m and y = 0–1.5 m and at x = 3.5–4.5 m (Fig. 10b) in the base layer. When this horizontal slice is compared with the correspondent GPR time-slices (Fig. 10c and d), the resistive anomalies are clearly superimposed by high-energy zones. These evidences could be attributed to a more inhomogeneous composition of the base layer or to a structural defect occurring at the interface between the concrete slabs and the base layer. The main disadvantages of these techniques are the huge amount of time needed for investigating a small area (about 30 min for a single array) and the limited depth of penetration (up to 0.9 m using a 16 × 3 electrodes configuration).

Besides the geometrical characterization of the pavement and the identification of anomalous zones due to a difference between the as-built and the original design or to a structural failure phenomena occurring below the concrete slabs, the airport Authority needs to estimate the stiffness properties (e.g. elastic modulus, Poisson's ratio) in order to evaluate if the pavement has maintained the original bearing capacity. The seismic refraction tomography can fulfill this target as long as it is focused only on anomalous zone where the mechanical parameters differ from those early assessed on undisturbed areas. Unfortunately,
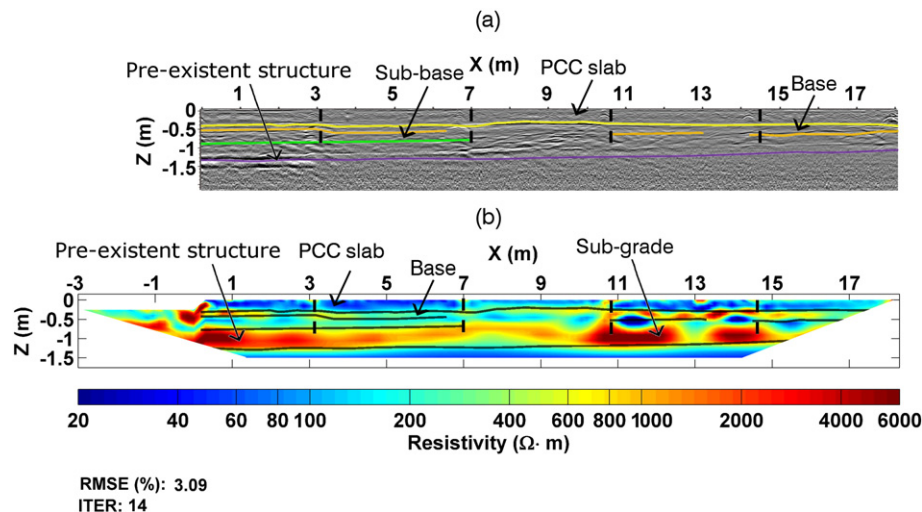

Fig. 7. (a) GPR vertical profile on L3 line for the 600 MHz antenna. The layers are marked in yellow (slabs), orange (base), green (subbase) and purple (subgrade). (b) Inverted model of ERT line L3. The direction of the line and the position of the first electrode is shown in Fig. 1. The layers are marked in black. Slab joints are indicated by dashed lines.
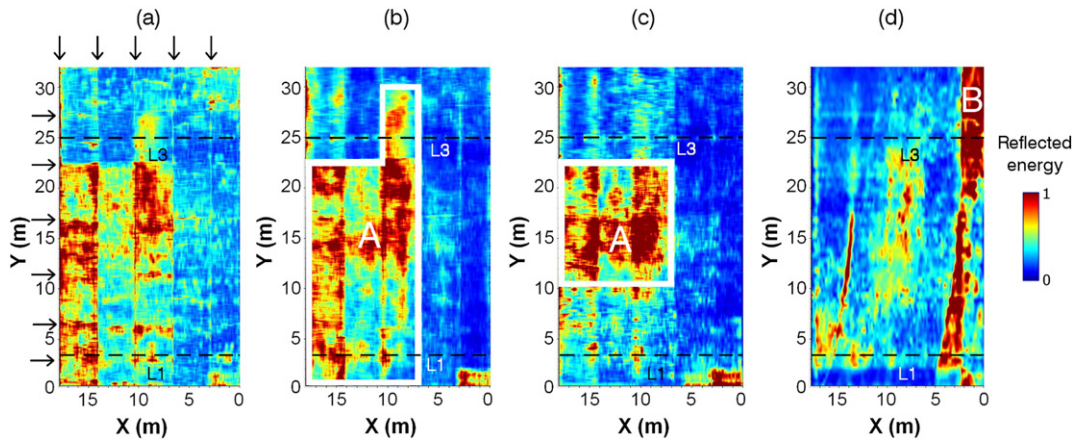
Fig. 8. Time-slice drawn for the GPR dataset. The L1 and L3 alignments are indicated with black dashed lines. (a) Time-slice at a depth of 0–30 cm for the 900 MHz antenna. Slab joints are indicated by black arrows. (b) Time-slice at a depth of 30–60 cm for the 900 MHz antenna. The high-energy zones is marked as "A", similarly to the EM evidence in Fig. 5a. (c) Time-slice at a depth of 60–90 cm for the 900 MHz antenna. The high-energy zone is marked as "A", similarly to the EM evidence in Fig. 5a. (c) Time-slice at a depth of 90–120 cm for the 200–600 MHz antennas. The high-energy zone is marked as "B", similarly to the EM evidence in Fig. 5a and b.

this kind of survey is still not rapid and low-budget, especially for high-resolution investigation (30 × 30 cm grid) as it needs a further effort to mechanize the source-receiver system. The results of the seismic tomography, performed on line L1 in Fig. 1, are shown in Figs. 11 and 12. In Fig. 11a and b two example shot gathers are reported for both P-Wave and S-Wave seismic tomography lines respectively, where good quality first arrivals could be picked for both surveys. For SH waves, picking of the S-wave arrival is enhanced by overlapping two opposite polarity records at each shot location. Where the Fourier amplitude spectrum of the above-cited seismograms are displayed (Fig. 11c and d for P- and S-wave respectively), it can be noticed that the relevant frequency content of the seismic signals is mainly distributed around 400–600 Hz for P-wave and 100–200 Hz for S-Wave seismograms, respectively.

The initial models for tomographic inversion of P- and S-wave dataset reflect the effective layering recovered by the above mentioned techniques, under the hypothesis of a velocity inversion passing from the slabs (Fiber Reinforced Concrete, conductive in ERT models) to the base layer (resistive in ERT models), while the seismic velocities of subbase layer (conductive) are supposed to be higher than the previous ones. The models are limited to a depth of 0.9 m corresponding to the subbase-subgrade interface, because the subgrade and the soil have lower stiffness than the overlying structure.

The results of the P-wave (first arrival) seismic tomography are displayed in Fig. 12a. Through the tomographic inversion of seismic data we reconstruct a P-wave velocity (V_P) for the concrete slab of about 2000 m/s, while the P-Wave velocities of the underlying layers are 1600 m/s (base) and 2300 m/s (subbase). There are only moderate changes in the V_P distribution within the model, principally due to the presence of the slab joints, even though the base layer seems to be affected by a higher variability, notably at x = 6–10 m and at x = 15–16 m, similarly to the GPR and ERT evidences (Figs. 6 and 8b).

The shear-wave tomography (Fig. 12b) has confirmed the same layering, with S-wave velocities ranging from about 1250–1300 m/s for slabs to about 900 and 1450 m/s for base and subbase. The S-wave model seems to be more diagnostic than the P-wave model, with respect to the velocity variation within each layer, detecting a low-velocity zone in the subbase layer at x = 10 accordingly to the ERT and GPR sections. The relative Root Mean Square Error (RMSE) for the two models is satisfactory, considering that the average travel time is about 1.5 ms and consequently the absolute RMSE is on the order of 0.2 ms, slightly higher than the random error committed by the operator during the picking procedure.

The resulting Poisson's ratio (σ) is given by the following formula:

$$\sigma = 0.5 \frac{\beta^2 - 2}{\beta^2 - 1} \qquad (6)$$

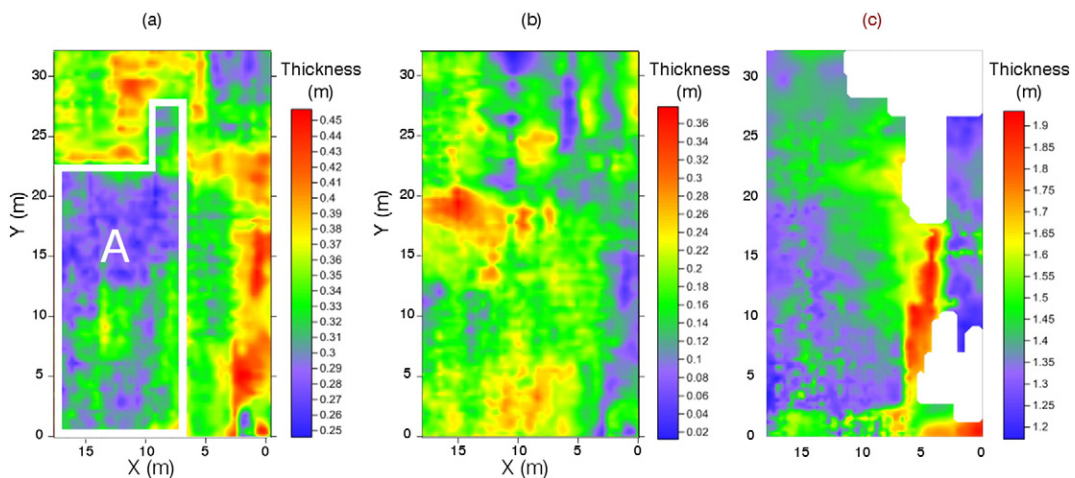where β is the ratio between V_P and V_S.

Fig. 9. Effective thicknesses of the pavement layers as resulting from the picking of the arrival time. (a) Thickness of slabs. The area delimited by white line corresponds to the anomalous zone "A" detected by the time-slice in Fig. 7b. (b) Thickness of the base layer. (c) Thickness of the whole pavement system (four layers).
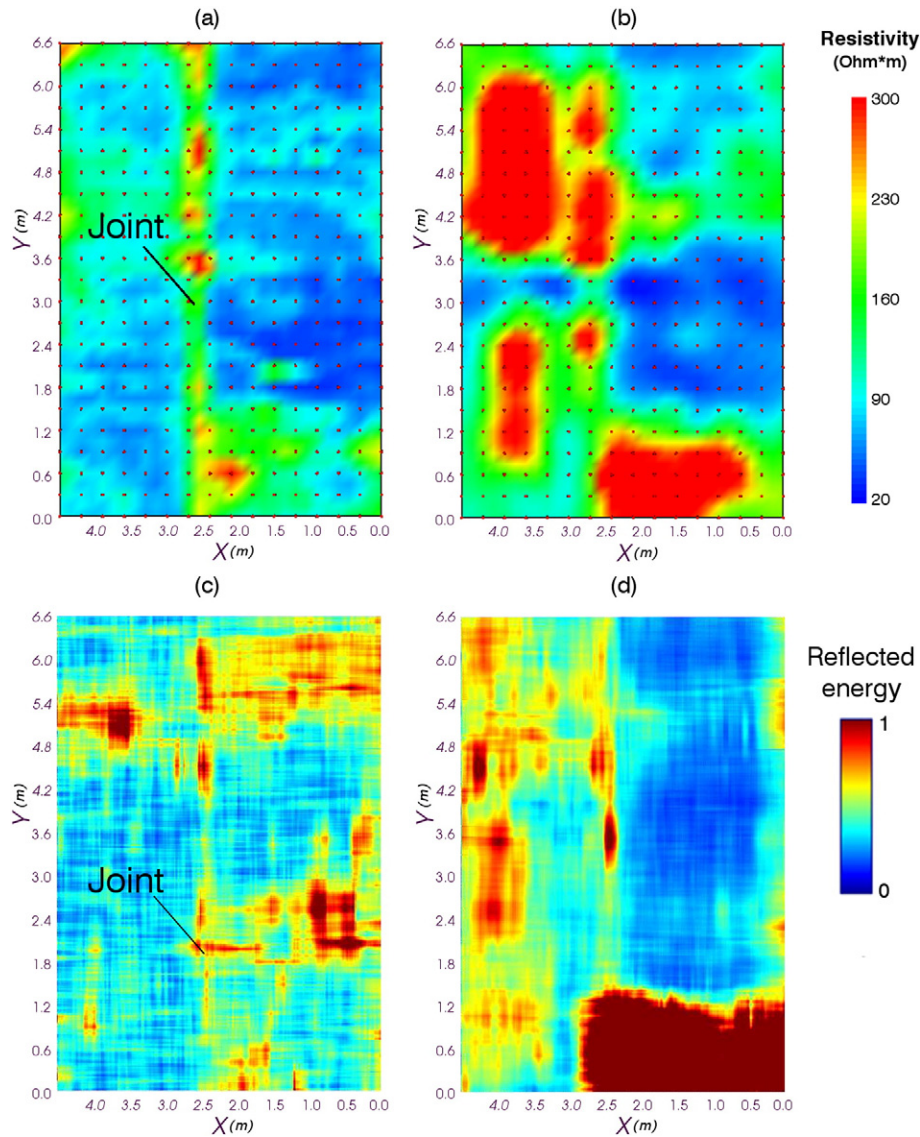
Fig. 10. Horizontal sections drawn at a depth of 15 (a) and 40 cm (b) from 3D ERT on the area indicated in Fig. 1. Data inversion is performed using the ErtLab© software. GPR time-slice at a depth of 0–30 cm (c) and 25–55 cm (d) on the same area of 3D ERT.

The slab n.1 and the asphalt zone are characterized by a low seismic ray coverage: consequently σ was evaluated only for the first layer. Hence we retrieve an average Poisson's ratio distribution, displayed in Fig. 12c, according to the pavement layering. The concrete slabs have a σ of 0.1–0.2, while for the base and the subbase σ is 0.25–0.28 and 0.17–0.23 respectively. These values are consistent with those recovered in literature on Portland Cement Concrete (slabs) and on a cement stabilized (base and subbase layer).

To evaluate the soil stiffness and to seek for independent confirmation of the tomography section, we compared a full waveform synthetic simulation with the tomographic inversion results. A 48-channel synthetic shot gather with the same geometrical characteristics of the seismic line is simulated by reflectivity modeling over a 1D model which is representative of the inverted tomographic section. We used a vertical surface point source with a Ricker embedded source wavelet having a frequency peak of 600 Hz. The 1D model was chosen averaging the results over the tomographic section, excluding the receivers over the asphalt. The compressional velocity of the three layers is set, from top to bottom, as 2000 m/s, 1650 m/s and 2300 m/s, respectively, whereas for the S-wave velocity values are: 1300 m/s, 900 m/s and 1450 m/s from top to bottom. The layer thickness is chosen as compliant to the

original pavement design (Fig. 1). Although it is recognized (Park et al., 2001) that proper investigation of the uppermost layers of a pavement structure requires a different acquisition system capable of handling much higher frequencies (>2000 Hz), the comparison may confirm anyway that the main characteristics of the observed spectra can be effectively predicted by full waveform modeling.

In Fig. 13 we display the results of this comparison in terms of the vertical component of particle velocity. In Fig. 13a we report the phase velocity vs frequency (or phase-shift) spectrum of an example shot gather of the experimental data. The frequency-phase velocity (*f-c*) spectrum of the synthetic shot gather is reported in Fig. 13b. The open black circles superimposed on the spectra indicate the ensemble of the experimental dispersion points (maxima of the *f-c* spectrum) averaged over all the shots of the seismic line. The main characteristics of the synthetic spectrum (Fig. 13b) are consistent with the observed one (Fig. 13a) and therefore confirms independently the pavement structure and layer velocities as pointed out by seismic tomography, which in principle may be affected by apparent velocity and hidden-layer problems in the case of velocity reversals. At the higher frequencies (>1000 Hz) the lack of correlation on the observed spectrum is due to the low frequency of the employed geophones (40 Hz).
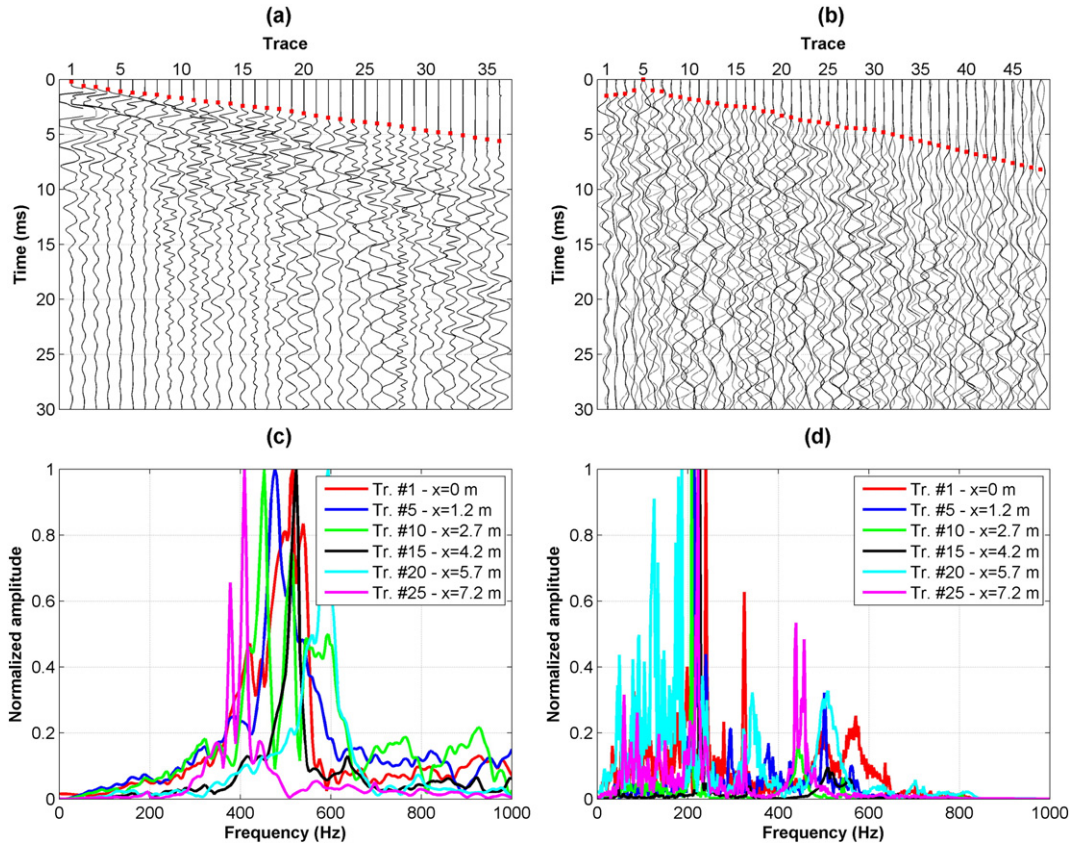
Fig. 11. (a) P-Wave seismogram for shot number 2 (x = 0 m) with picked P-wave arrivals. (b) SH-Wave seismogram for shot number 4 (x = 1.2 m) with picked SH-wave arrivals. Solid black line and solid gray line correspond to the opposite shot direction. (c) Fourier amplitude spectrum of selected traces for the P-Wave seismogram. (d) Fourier amplitude spectrum of selected traces for the SH-Wave seismogram.
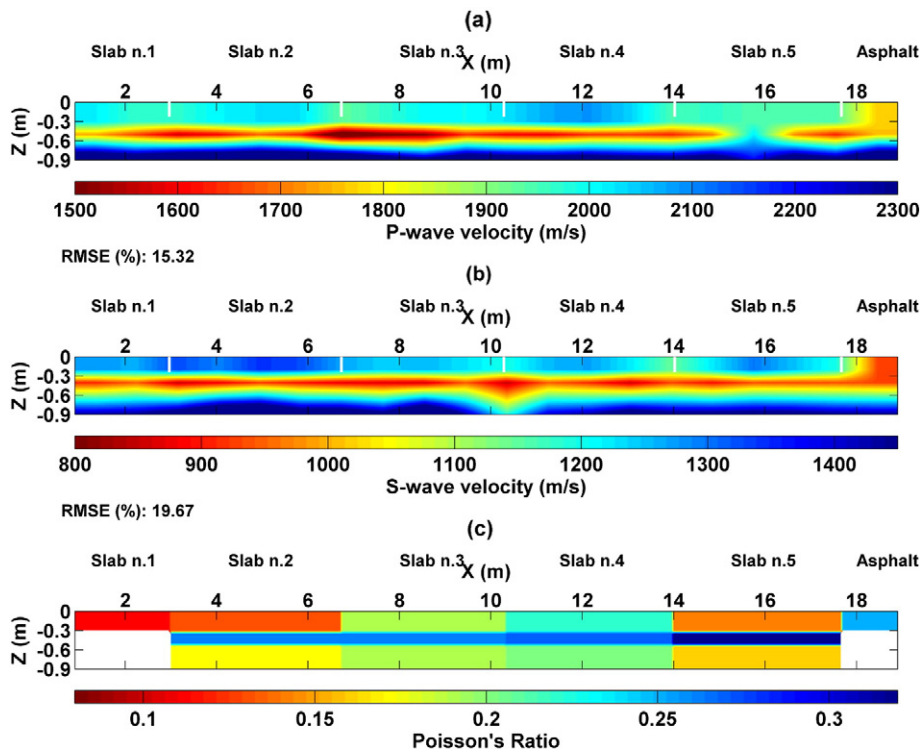

Fig. 12. (a) Inverted model of the P-Wave seismic line L1. (b) Inverted model of the SH-Wave seismic line L1. (c) Poisson's Ratio section derived from the inverted seismic models.
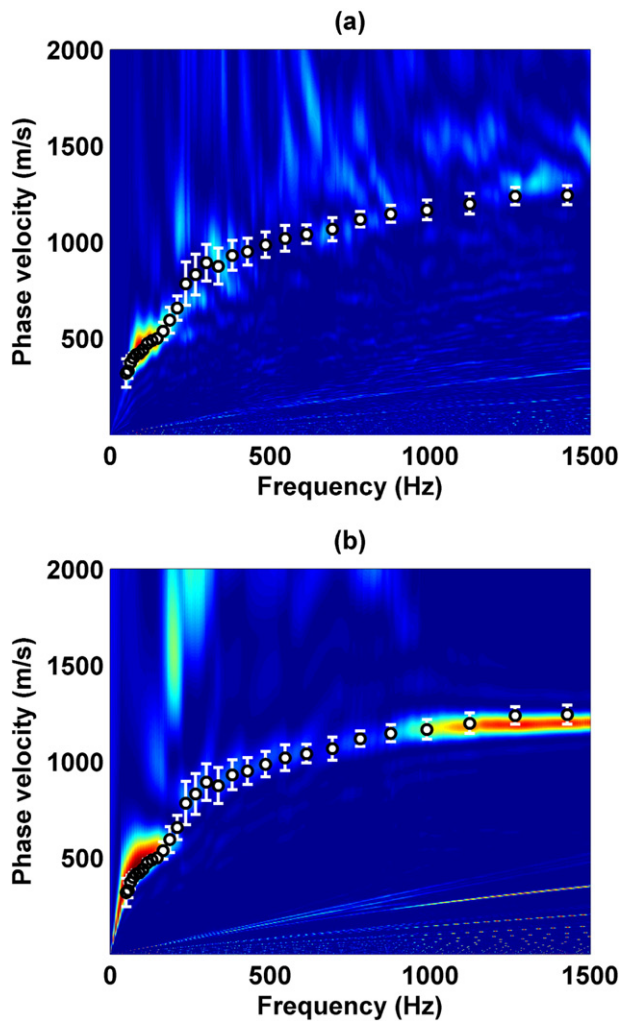
Fig. 13. (a) Phase velocity-frequency spectrum of an example shot gather for the experimental dataset. (b) Phase velocity-frequency spectrum of an example shot gather for the synthetic dataset. Open black circles indicate the experimental dispersion points.

5. Discussion and conclusions

The integration of well-developed geophysical methods (electromagnetic, georadar, electrical and seismic) can be an important tool where the integrity and reliability of an airport pavement have to be assessed. These methods are cost-effective and can be used to map extensively the pavement during the verification tests to be performed at the end of the work, in order to discriminate critical areas or areas where the as-built differs from the original design.

In addition to the GPR method, an established technique for these applications, the high-resolution electrical and seismic methods can give a further contribution in order to retrieve geometric, physical and mechanical parameters of the pavement.

In particular, the geophysical campaign has validated the layout deduced form the original design and formed by four layers having a medium thickness of about 30, 20, 40 and 60 cm respectively, each characterized by a high degree of variability in both the x- and y-directions. The first layer, consisting of PCC slabs, probably fiber reinforced, is relatively homogeneous and characterized by low resistivity (about 30–40 Ωm) and a Poisson's ratio around 0.15. The base layer covering the entire area at depths ranging from 30 to 50 cm is more inhomogeneous, as it remains undistinguishable in some areas from the underlying layer and exhibits a different physical characteristics (resistivity of about 200–600 Ωm and Poisson's ratio of 0.27), related to a less rigid and more porous material. The subbase layer presents a resistivity of about 100 Ωm and a Poisson's ratio of 0.2. The Poisson's ratios of the three layers are consistent with values recovered in literature for pavement materials. Below this three-layered pavement, we detected a resistive layer (subgrade) and a homogenous low resistivity value (40–50 Ωm) related to the in-situ silty sands deposits. The ERT and SRT methods have provided reliable inverted models, with low RMSE values displayed at the final iteration.

The EM method returns only a low-resolution image of the pavement, although very rapid and cost-effective. It can be employed for a quick screening of the airfield, where a high degree resolution is not required. On the contrary, GPR can give a high-resolution image of the investigated pavements, where the time necessary to investigate a fixed area remains approximately unchanged with respect to the EM. Nevertheless the detected anomalies cannot be always properly addressed and it could be difficult to give an unambiguous cause-and-effect relationship in the absence of a-priori or additional information. An advanced processing, based the picking of the arrival times (eliminating what is derived by the interpolation) can give a more quantitative information about the deviation between the design and the as-built thickness of layers (whose mean value shall not be lower by >5% compared to the original design). Therefore it can be an important tool for engineers and professionals involved in the final testing procedure of the structure.

Some major issues, previously highlighted for GPR, can be fulfill by ERT, to be executed along 2D alignment conveniently spaced, since the 3D configuration is still not rapid as it requires about 30 min for acquiring a single dataset with a widespread used resistivimeter.

Although the pavement layers were well-recognized and modeled using all the two above mentioned methods, the ERT suffers of loss in resolution in depth and the GPR signal strength is adequate only for depth up to about 1–1.5 m. As a matter of fact the anomalies detected by each technique are consistent among them and they can be correlated to failure phenomena occurring at interfaces between layers or to an inhomogeneous thickness of the different layers. However we still has not found for this site a clear causal relationship between these anomalies and the surface evidences (fractures) Where an elastic characterization is needed for assessing the maximum vertical load, the seismic refraction tomography has the substantial advantage, with respect to the Falling Weight Deflectometer (FWD), to directly calculate velocity values and consequently the Poisson's ratio at small intervals throughout the pavement. This lead to a high-resolution reconstruction of the analyzed pavement as compared with the low-resolution obtained by the FWD, whereas a more detailed mapping can be obtained only with a non-linear increase of the operational costs.

On the other hand, since the seismic methods are not always rapid, especially for a high-resolution multi-shot tomography, it needs a further improvement towards the developing of a mechanized and continuous system including source, streamer and cables, and acquisition systems capable of handling much higher frequencies than the conventional geophysical acquisition systems, sources and receivers.

Therefore, GPR and EM can be extensively used to derive the effective layering, both referring to the thickness of the concrete slab and to the thickness and the degree of conservation of the underlying materials. In more detail 2D and/or 3D ERT arrays can be applied to unequivocally identify the anomalous zones, early individuated by a large GPR screening, where higher values of resistivity would be associated to the more porous and prone to breaking zones. Then a more focused investigation on selected areas should comprehend a SRT survey for retrieving the mechanical parameters. This approach on field investigations could be further improved by monitoring the physical and mechanical parameter in time for maintenance and in order to avoid the occurrence of critical conditions on the structure.

References

Al-Qadi, I.L., Lahouar, S., 2005. Measuring layer thicknesses with GPR–theory to practice. Constr. Build. Mater. 19, 763-2.

Al-Qadi, I.L., Lahouar, S., Loulizi, A., 2001. In situ measurements of hot-mix asphalt dielectric properties. NDT&E Int. 34, 427-4.

American Society of Testing Materials, 2008. Standard test method for evaluating asphalt-covered concrete bridge decks using ground penetrating radar. Designation D 6087-08. ASTM International, West Conshohocken, PA.

Asakawa, E., Kawanaka, T., 1993. Seismic ray tracing using linear travel time interpolation. Geophys. Prospect. 41, 99-1.

Benedetto, A., Benedetto, F., 2011. Remote sensing of soil moisture content by GPR signal processing in the frequency domain. IEEE Sensors J. 10, 2432–2441.

Benedetto, A., Benedetto, F., Tosti, F., 2012. GPR applications for geotechnical stability of transportation infrastructures. Nondestruct. Test. Eval. 27, 253–262.

Benedetto, F., Tosti, F., 2013. GPR spectral analysis for clay content evaluation by the frequency shift method. J. Appl. Geophys. 97, 89–96.

Buettner, M., Ramirez, A., Daily, W., 1996. Electrical resistance tomography for imaging the spatial distribution of moisture in pavement sections. Structural Materials Technology an NDT Conference. Lawrence Livermore National Laboratory, University of California, San Diego, CA.

Cardarelli, E., Cerreto, A., 2002. Ray tracing in elliptical anisotropic media using linear traveltime seismic interpolation (LTI) method applied to traveltime seismic tomography. Geophys. Prospect. 50, 55-2.

Cardarelli, E., de Nardis, R., 2001. Seismic refraction, isotropic and anisotropic seismic tomography on an ancient monument. Geophys. Prospect. 49, 228.

Cardarelli, E., Fischanger, F., 2006. 2D data modelling by electrical resistivity tomography for complex subsurface geology. Geophys. Prospect. 54, 121–123.

Cardarelli, E., Cercato, M., De Donno, G., 2014. Characterization of an earth-filled dam through the combined use of electrical resistivity tomography, P-and SH-wave seismic tomography and surface wave data. J. Appl. Geophys. 106, 87-5.

Cardarelli, E., Fischanger, F., Piro, S., 2008. Integrated geophysical survey to detect buried structures for archaeological prospecting. A case-history at Sabine Necropolis (Rome, Italy). Near Surf. Geophys. 6, 15.

Clark, M.R., McCann, D.M., Forde, M.C., 2003. Application of infrared thermography to the non-destructive testing of concrete and masonry bridges. NDT&E Int. 36, 265.

De Beer, M., 1990. In: Blight, et al. (Eds.), Use of Dynamic Cone Penetrometer (DCP) in the Design of Road Structures. Geotechnics in African Environment, Balkema, Rotterdam.

De Donno, G., 2013. 2D tomographic inversion of complex resistivity data on cylindrical models. Geophys. Prospect. 61, 586-1.

Drahor, M.G., 2006. Integrated geophysical studies in the upper part of Sardis archaeological site, Turkey. J. Appl. Geophys. 59, 205-3.

Goel, A., Das, A., 2008. Nondestructive testing of asphalt pavements for structural condition evaluation: a state of the art. NDT&E Int. 23, 121-0.

Gordon, M.O., Broughton, K., Hardy, M.S.A., 1998. The assessment of the value of GPR imaging of flexible pavements. NDT&E Int. 31, 429-8.

Kim, J.R., Kang, H.B., Kim, D., Park, D.S., Kim, W.J., 2007. Evaluation of in situ modulus of compacted subgrades using portable falling weight deflectometer and plate-bearing load test. J. Mater. Civ. Eng. 19, 492–499.

Liu, H., Sato, M., 2014. In situ measurement of pavement thickness and dielectric permittivity by GPR using an antenna array. NDT&E Int. 64, 65-1.

Loizos, A., Plati, C., 2007. Accuracy of pavement thicknesses estimation using different ground penetrating radar analysis approaches. NDT&E Int. 40, 147.

Malagodi, S., Orlando, L., Piro, S., Rosso, F., 1996. Location of archaeological structures using GPR method: three-dimensional data acquisition and radar signal processing. Archaeol. Prospect. 3, 13.

Maser, K.R., Holland, T.J., Roberts, R., Popovics, J., 2006. NDE methods for quality assurance of new pavement thickness. Int. J. Pavement Eng. 7, 1-0.

McNeill, J.D., 1980. Electromagnetic terrain conductivity measurement at low induction numbers. Technical Note TN-6. Geonics Ltd, Mississauga, ON.

Mesher, D.E., Dawley, C.B., Davis, J.L., Rossiter, J.R., 1995. Evaluation of new ground penetrating radar technology to quantify pavement structures. Transp. Res. Rec. 1505, 17-6.

Mohammadi, S.D., Nikoudel, M.R., Rahimi, H., Khamehchiyan, M., 2008. Application of the Dynamic Cone Penetrometer (DCP) for determination of the engineering parameters of sandy soils. Eng. Geol. 101, 195-3.

Moropoulou, A., Avdelidis, N.P., Koui, M., Kakaras, K., 2001. An application of thermography for detection of delaminations in airport pavements. NDT&E Int. 34, 329-5.

Moskalyuk, O.A., Aleshin, A.N., Tsobkallo, E.S., Krestinin, A.V., Yudin, V.E., 2012. Electrical conductivity of polypropylene fibers with dispersed carbon fillers. Phys. Solid State 54, 2122–2127.

Nazarian, S., Yuan, D., Tandon, V., 1654. Structural field testing of flexible pavement layers with seismic methods for quality control. Transp. Res. Rec. 1999, 50.

Neubauer, W., Eder-Hinterleitner, A., Seren, S., Melichar, P., 2002. Georadar in the roman civil town Carnuntum, Austria: an approach for archaeological interpretation of GPR data. Archaeol. Prospect. 9, 135–136.

Orlando, L., Slob, E., 2009. Using multicomponent GPR to monitor cracks in a historical building. J. Appl. Geophys. 67, 327-4.

Orlando, L., 2005. Joint interpretation of geophysical data for archaeology: a case study. Subsurf. Sens. Technol. Appl. 6, 235.

Papadopoulos, N.G., Yi, M.J., Kim, J.H., Tsourlos, P., Tsokas, G.N., 2010. Geophysical investigation of tumuli by means of surface 3D electrical resistivity tomography. J. Appl. Geophys. 70, 192–195.

Park, C.B., Ivanov, J., Miller, R.D., Xia, J., Ryden, N., 2001. Multichannel analysis of surface waves (MASW) for pavement-feasibility test. Proceedings of the 5th SEGJ International Symposium. The Society of Exploration Geophysicists of Japan (SEGJ), Tokyo, Tokyo, p. 25-0.

Piro, S., Goodman, D., Nishimura, Y., 2003. The study and characterization of emperor Traiano's villa (Altopiani di Arcinazzo, Roma) using high-resolution integrated geophysical surveys. Archaeol. Prospect. 10, 1–5.

Ryden, N., Park, C.B., 2006. Fast simulated annealing inversion of surface waves on pavement using phase-velocity spectra. Geophysics 71, R49-8.

Ryden, N., Park, C.B., Ulriksen, P., Miller, R.D., 2004. Multimodal approach to seismic pavement testing. J. Geotech. Geoenviron. Eng. 130, 636-5.

Saarenketo, T., Scullion, T., 2000. Road evaluation with ground penetrating radar. J. Appl. Geophys. 43, 119-8.

Saarenketo, T., 1997. Using ground-penetrating radar and dielectric probe measurements in pavement density quality control. J. Transp. Res. Board 1575, 34-1.

Seo, J.W., Kim, S.I., Choi, J.S., Park, D.W., 2009. Evaluation of layer properties of flexible pavement using a pseudo-static analysis procedure of falling weight deflectometer. Constr. Build. Mater. 23, 3206-3.

Tholen, O., Sharma, J., Terral, R.L., 1985. Comparison of falling weight deflectometer with other deflection testing devices. Transp. Res. Rec. 1007, 131–134.

Tsokas, G.N., Tsourlos, P.I., Vargemezis, G., Novack, M., 2008. Non-destructive ERT for in-doors investigations: the case of Kapnikarea Church in Athens. Archaeol. Prospect. 15, 47-1.

Tsourlos, P.I., Tsokas, G.N., 2011. Non-destructive electrical resistivity tomography survey at the south walls of the acropolis of Athens. Archaeol. Prospect. 18, 173–176.

Vaughan, C.J., 1986. Ground-penetrating radar surveys used in archaeological investigations. Geophysics 51, 595-4.

Wolke, R., Schwetlick, H., 1988. Iteratively reweighted least squares: algorithms, convergence analysis, and numerical comparisons. SIAM J. Sci. Stat. Comp. 9, 907-1.

Won, I.J., Huang, H., 2004. Magnetometers and electro-magnetomenters. Lead. Edge 23, 448-1.